Applied Surface Science Advances 12 (2022) 100349

Contents lists available at ScienceDirect

Applied Surface Science Advances

journal homepage: www.sciencedirect.com/journal/applied-surface-science-advances

Mn-doped ZnO microspheres prepared by solution combustion synthesis for room temperature NH_3 sensing

Asha Ramesh [a], D.S. Gavaskar [b], P. Nagaraju [c], Suryakala Duvvuri [d], S.R.K. Vanjari [e], C. Subrahmanyam [a,*]

[a] Department of Chemistry, Indian Institute of Technology Hyderabad, Kandi, Sangareddy, Telangana 502285, India
[b] Department of Physics, Osmania University, Amberpet, Hyderabad, Telangana 500007, India
[c] Department of Physics, CMR Technical Campus, Kandlakoya, Hyderabad, Telangana 501401, India
[d] Department of Chemistry, GITAM University, Visakhapatnam, Andhra Pradesh 530045, India
[e] Department of Electrical Engineering, Indian Institute of Technology Hyderabad, Kandi, Sangareddy, Telangana 502285, India

ARTICLE INFO

Keywords:
Ammonia
Gas sensor
Transition metal doping
Surface acidity
Mn-doped ZnO
Room temperature sensing

ABSTRACT

Despite being the most favorable ammonia (NH_3) gas sensors, metal oxide semiconductors fail to deliver high selectivity and room temperature (RT) sensing. Tuning the metal oxide with doping is an attractive way of overcoming these disadvantages. Herein, we report Mn-doped ZnO microspheres as promising sensors for highly sensitive and selective RT sensing of NH_3. ZnO and 2 wt% Mn-doped ZnO microspheres were synthesized by a low-cost and fast solution combustion synthesis, and their structure, morphology, and gas sensing properties were investigated. Mn-doping resulted in a change in the lattice parameters, an increase in the oxygen vacancies, and surface acidity of ZnO as confirmed by X-ray diffraction (XRD), X-ray photoelectron spectroscopy (XPS) and Temperature programmed desorption (TPD), respectively. Mn-doped ZnO showed a response (R_a/R_g) of 20.2 in 100 ppm NH_3, which is significantly higher than ZnO. The sensor showed high selectivity, three times higher than that of ZnO, and good stability. Improvement in the sensing performance of Mn-doped ZnO is attributed to the increase in the defects and surface acidity with Mn-doping.

Introduction

The ever-advancing industrialization has led to increased emissions of gases into the environment. Detection of these gases is important to monitor and control their impact on life and the environment [1]. Among the various gases, ammonia (NH_3) is a corrosive and highly toxic gas that can cause harmful effects on human life if inhaled above the threshold [2]. NH_3 gas is actively used in several industries to produce many chemicals including explosives, plastics, dyes, fertilizers, etc. The increased use of NH_3 has led to increased emissions of gas into the environment. In addition, it is highly flammable at concentrations between 16-28% by volume in air. Due to its low density and corrosive nature, an NH_3 gas leak can have more serious effects on the exposed area. NH_3 gas is also a potential biomarker for diagnosing health conditions such as kidney failure, gastric infections, etc. The development of highly sensitive, selective, and accurate low-cost NH_3 gas sensors is necessary to monitor its concentration in view of the threat to life and the environment. NH_3 sensors find applications in areas such as environmental protection, workplace safety, transportation, and process control in industry, agriculture, and health.

Electrochemical, optical, calorimetric, capacitance based, metal oxide based, and acoustic wave based are different technologies used for NH_3 gas sensing [3–9]. Among all these methods, semiconductor metal oxide gas sensors have the greatest advantage because of their high sensitivity, fast response, low-cost, long stability, and ease of manufacture [10,11]. Metal oxide gas sensors detect NH_3 gas by measuring the change in resistance that occurs when analyte gas is nearby. With the advancement of nanoscience and nanotechnology, the synthesis and use of these materials at nanoscale became easier and contributed to the improvement of sensors due to the excellent properties of nanomaterials, such as the high surface area to volume ratio and electrical properties [12–16]. The dimensions and surface morphologies of different nano metal oxides affect sensor performance. Therefore, various synthesis methods like chemical vapor deposition, co-precipitation [17], sol gel method [18–21], hydrothermal method, etc [22–25] can be used to control the properties of the sensor material.

* Corresponding author.
E-mail address: csubbu@iith.ac.in (C. Subrahmanyam).

https://doi.org/10.1016/j.apsadv.2022.100349
Received 21 June 2022; Received in revised form 31 October 2022; Accepted 18 November 2022
Available online 24 November 2022

ZnO, SnO_2, TiO_2, WO_3, and MoO_3 are widely explored metal oxides for detecting NH_3 gas [26–30]. Among these metal oxides, ZnO has attracted much attention because of its excellent electrical and chemical properties [31,32]. ZnO is an n-type semiconductor metal oxide with a significant exciton binding energy of 60 meV and a band gap of 3.37 eV [33]. But ZnO sensor performance has limitations in terms of sensitivity, selectivity, and working temperature [34] which can be improved by various methods such as doping and surface modifications [35]. Doping transition metals or composites with metal oxides improve gas sensing properties. Rambu et al. obtained Ni-doped ZnO films by spin coating and showed a higher sensor response to NH_3 than pure ZnO films at a temperature of 190 °C. The improvement was attributed to the morphostructural changes induced by the addition of Ni into the ZnO structure [36]. Tarwal et al. prepared Cd-doped ZnO thin films by spray pyrolysis and showed an increased response to NH_3 compared to the ZnO thin films [37]. Using the same fabrication method, Mani et al. fabricated Ni-doped ZnO thin films and demonstrated the selective detection of NH_3 [38]. Ganesh et al. used hydrothermal synthesis to prepare Cu-doped ZnO nanoellipsoids, which showed improved sensitivity to NH_3 gas and good selectivity at 150 °C compared to ZnO [39]. Mani et al. showed that spray deposited Co-doped ZnO thin films reduced the ZnO response to NH_3 but improved detection range and selectivity [40]. Zheng et al. used magnetic sputtering to fabricate Ag-doped ZnO nanostructured films. The superior performance of the sensors compared to pure ZnO film was explained by the larger surface area of the Ag-doped ZnO film [41]. However, most of these sensors require a high working temperature and have low selectivity.

The acid-base and redox reactions that occur on the surface of the sensor material contribute to the sensor signal, and the specificity or selectivity of these reactions depends on the nature of the active sites on the surface [42]. Vorobyeva et al. synthesized Ga-doped ZnO and studied the effect of surface acidity on the sensitivity to H_2S and showed that increasing the surface acidity of Ga-doped ZnO decreases the response to H_2S due to its acidic nature [43]. Previous studies reported that an increase in the surface acidity of the sensor material helps in the highly selective determination of a basic NH_3 gas [44,45]. However, few reports are available correlating acid-base properties with gas sensing.

Mn-doping in ZnO has attracted significant research interest due to its ferromagnetic properties at room temperature (RT) and is attributed to the increase in defects resulting from Mn-doping. Doping and surface defects are also important to improve the gas sensing properties of semiconductor metal oxides [46]. Still, there are not many studies on using Mn-doped ZnO for NH_3 gas sensing. In addition, because of the similar sizes of Mn^{2+} and Zn^{2+} cations, Mn is more easily incorporated into the ZnO lattice than other transition metals. Many of the transition metal doped ZnO for NH_3 detection are on thin films and use expensive techniques and they operate at a higher temperature. In the present work, we report a fast and low-cost solution combustion synthesis to introduce lower Mn-doping (2 wt%) to improve the NH_3 sensing properties of ZnO at RT. The sensitivity and selectivity of Mn-doped ZnO were improved at RT. The acid-base nature of the materials was studied using NH_3 and CO_2 temperature programmed desorption (TPD). The importance of surface acidity and surface defects correlates with improved sensor properties.

Experimental section

Materials

Manganese nitrate tetrahydrate ($Mn(NO_3)_2.4H_2O$, 97%, Sigma - Aldrich), Zinc nitrate hexahydrate ($Zn(NO_3)_2.6H_2O$, 99%, Sigma - Aldrich), Urea (CH_4N_2O, 99%, SRL Chemicals), and Silver conductive paste (Ag, 99.9%, Sigma - Aldrich). All chemicals were of analytical purity and were used without further purification.

Synthesis procedure

The ZnO and Mn-doped ZnO (2 wt%) were prepared via a simple solution combustion synthesis. To prepare the ZnO, 1g $Zn(NO_3)_2.6H_2O$ was taken in 15 mL distilled water in a China dish and dissolved under sonication. 401 mg of urea was added to the above solution and then sonicated for 15 min. The reaction mixture was transferred to a muffle furnace which was preset at a temperature of 450 °C for a period of 10 min to obtain ZnO [47]. The product was cooled to RT and calcined at 600 °C for 3 hrs. The same procedure was used to synthesize Mn-doped ZnO by taking 20 mg of $Mn(NO_3)_2.4H_2O$ and 980 mg of $Zn(NO_3)_2.6H_2O$ in 15 mL of water. Fig. 1 shows a scheme for the synthesis of Mn-doped ZnO. The chemical equation for the synthesis is represented by Eq. (1).

$$3Zn(NO_3)_2.6H_2O + 5(NH_2)_2CO \rightarrow 3ZnO + 5CO_2 + 28H_2O + 8N_2 \quad (1)$$

Fabrication of sensor

A glass substrate (2 cm × 2 cm) was cleaned with acetone and dried in the oven. Silver contacts were made on the glass substrate using a brush and conductive silver paste and dried in an oven for one hour at 60 °C. 15 mg of the material was mixed into a paste with a few drops of methanol in a crucible using a glass rod. The prepared paste was applied between the silver electrodes on the glass substrate by drop coating. The device was dried at 100 °C overnight and was then used for gas sensing studies. A scheme for the fabrication of the sensor is shown in Fig. 2.

Characterization techniques

Powder X-ray diffraction (XRD) patterns of the prepared materials were recorded using a Rigaku SmartLab X-ray diffractometer using Cu Kα (λ=1.54 Å) radiation and a Ni filter. The measurement was recorded at ambient temperature conditions for a 2θ value of 20 to 80 degrees with a scan rate of 3 degrees/min. A current of 200 mA and an accelerating voltage of 45 kV are maintained during the measurements. The chemical composition of the materials and oxidation states of the elements were characterized by X-ray photoelectron spectroscopy (XPS) using Supra Kratos analytical spectrophotometer with Mg Kα monochromatic excited radiation of 1253.6 eV. The morphologies of the materials were examined by Field emission scanning electron microscopy (FESEM) by using the JEOL JIB-4700F multi-beam system at 3 kV operating potential. Elemental analysis of the samples was further performed by Energy dispersive X-ray spectroscopy (EDS) during FESEM characterization. FTIR studies were carried out in JASCO FT/IR-4600 with a resolution of 4 cm^{-1} in a range from 400 to 3000 cm^{-1}. Raman spectra of the materials were obtained using a WITEC alpha300 R – Raman Imaging microscope with a laser excitation wavelength of 532 nm. The acidic and basic groups on the surface of the materials were quantified using NH_3 TPD, and CO_2 TPD, respectively, using a MicrotracBEL Corp. chemisorption device equipped with a thermal conductivity detector. The samples (80 mg) were pretreated at 500 °C for 1 hr under He flow and then cooled down to 100 °C, and the adsorption of NH_3 was facilitated by flowing of NH_3/He of 5 vol% at this temperature. The chemisorbed NH_3 was desorbed by increasing the temperature of the sample to 800 °C at a constant heating rate of 10 °C/min under a He flow of 30 mL/min. CO_2 TPD was also performed by a similar method to examine the basic sites on the materials.

Gas sensing setup

The homebuilt setup used for the gas sensing measurements is shown schematically in Fig. 3. The resistance variations of the sensor over time were measured using a Keithley source meter (USA, model: 6517B). During the electrical characterization, a fixed voltage of 3 V is applied to the sensor and the current is monitored and recorded over time. A digital humidity controller (Humitherm, India) maintained the chamber at a

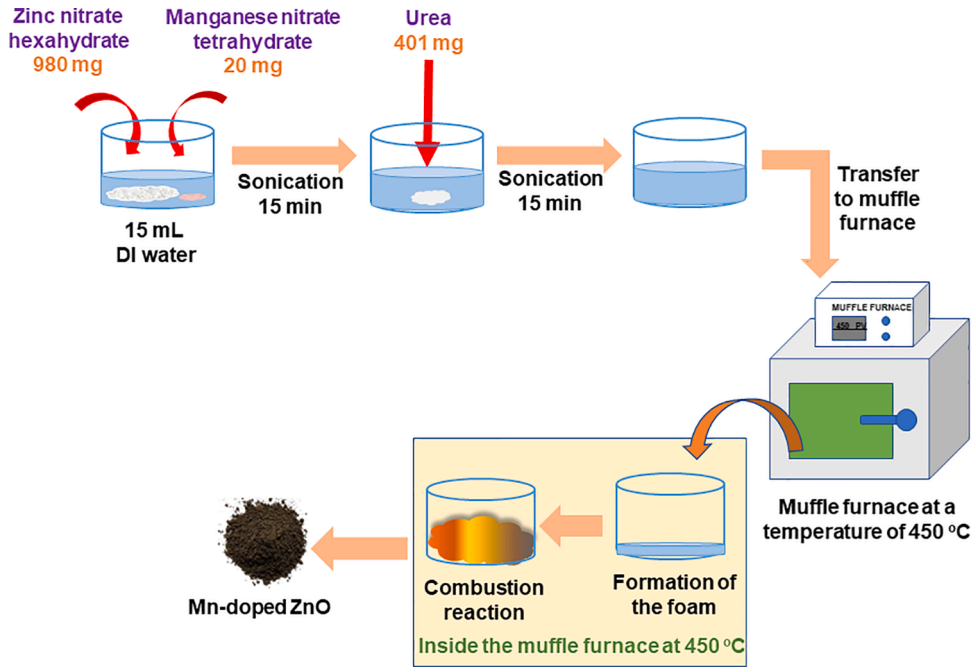

Fig. 1. Scheme for the synthesis of Mn-doped ZnO.

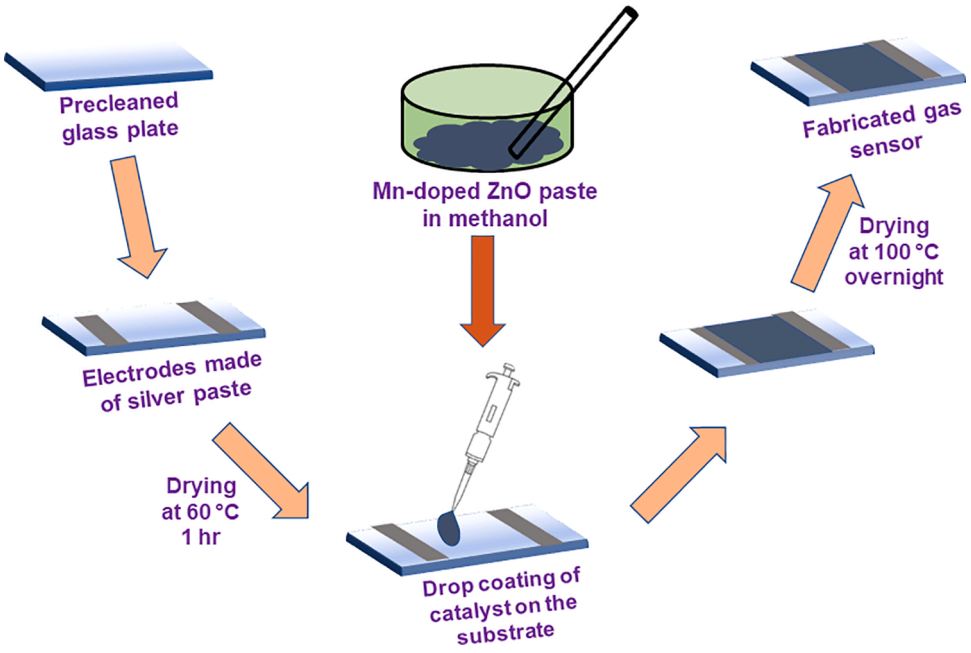

Fig. 2. Scheme for the fabrication of the Mn-doped ZnO gas sensor.

relative humidity of 60%. Air and the required ppm of analyte gases were then admitted to the chamber to record the baseline resistance and the resistance in the presence of analyte gas.

Results and discussion

X-ray diffraction

The crystal structures of ZnO and Mn-doped ZnO were monitored by XRD and are shown in Fig. 4a. It was observed that ZnO has a hexagonal wurtzite structure with space group P63mc with calculated cell parameters a = b = 3.24 Å, c = 5.19 Å and diffraction peaks at 2θ = 31.95°, 34.61°, 36.43°, 47.73°, 56.78°, 63.05°, 66.56°, 68.13°, 69.26° corresponding to the d values of 2.80, 2.59, 2.46, 1.90, 1.62, 1.47, 1.40, 1.37, 1.35 Å which align well with the (100), (002), (101), (102), (110), (103), (200), (112) and (201) crystalline planes respectively and match with JCPDS card number 36-1451 as shown in Fig. 4a. As shown in Fig. 4b, Mn-doped ZnO gave peaks corresponding to hexagonal wurtzite structure but with a slight shift to lower angles at 31.75°, 34.40°, 36.24°, 47.53°, 56.60°, 62.86°, 66.39°, 67.96°, 69.10° corresponding to the d values of 2.81, 2.60, 2.48, 1.91, 1.62, 1.48, 1.41, 1.38, 1.36 for the crystal planes (100), (002), (101), (102), (110), (103), (200), (112) and (201), respectively. The XRD spectra of Mn-doped ZnO showed no additional peak, implying that no secondary phase is formed and the

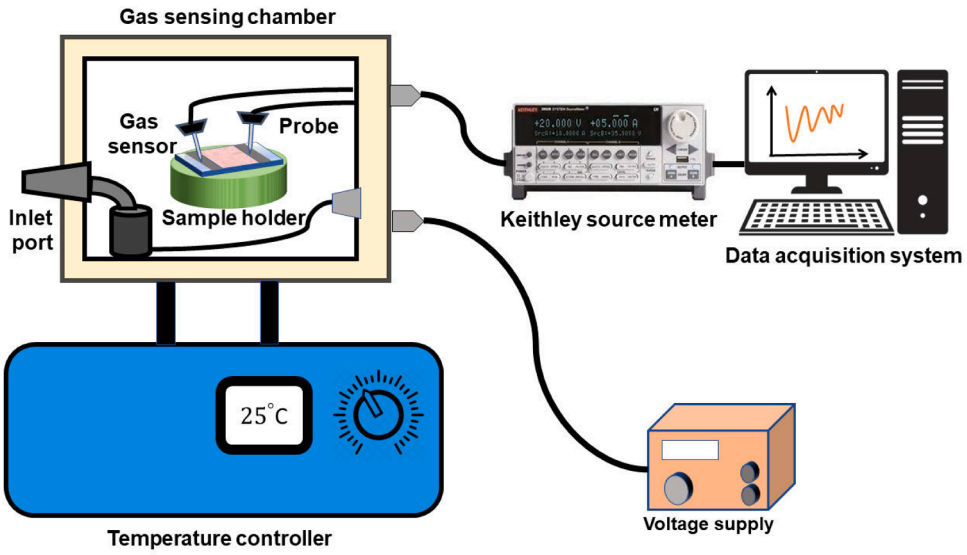

Fig. 3. Schematic representation of the gas sensing setup.

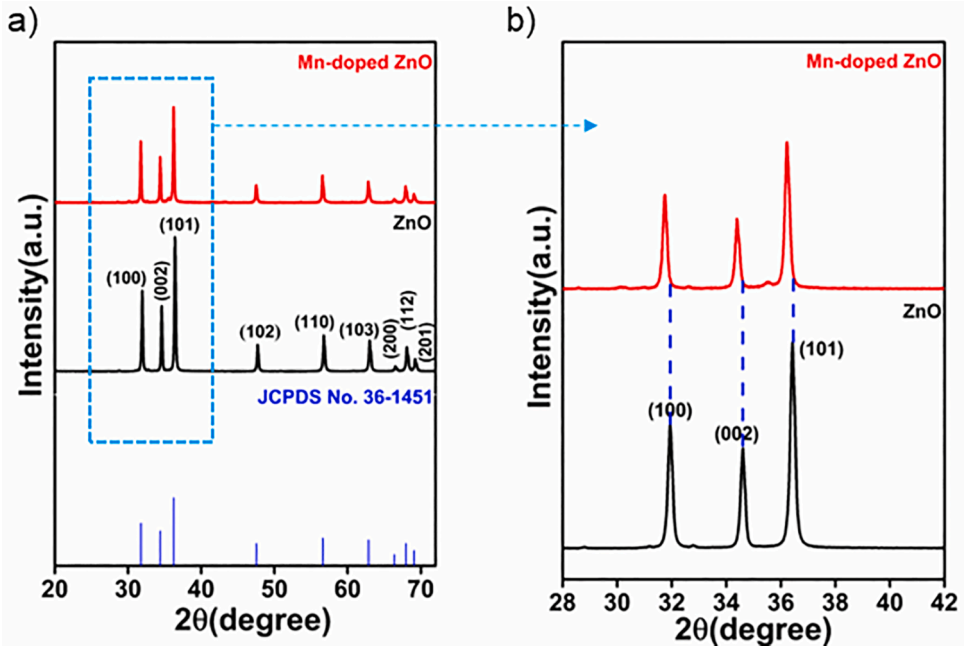

Fig. 4. (a) XRD patterns of ZnO and Mn-doped ZnO. (b) Shifting of the XRD peaks of Mn-doped ZnO in comparison with ZnO.

Mn^{2+} ions replace the Zn^{2+} ions in the ZnO lattice. Doping with Mn slightly increases the d spacing value. Lattice parameters of Mn-doped ZnO were found to be a = b = 3.25 Å, c = 5.21 Å. It shows that doping with Mn slightly increases the lattice parameters of ZnO without changing the hexagonal structure. The average crystallite size of the materials was calculated from XRD using Scherrer's formula $\left(t = \frac{K\lambda}{\beta Cos\theta}\right)$ where Scherrer constant (K) = 0.89, Cu K_α radiation wavelength (λ) = 1.5406 Å, β = FWHM, t = Average crystallite size and θ = Diffraction angle). ZnO, Mn-doped ZnO has an average crystallite size of 43.3 nm and 49.5 nm, respectively. The Mn^{2+} cation is slightly larger in size compared to Zn^{2+}, which leads to a change in the lattice parameters of ZnO when Mn^{2+} replaces Zn^{2+} in the lattice. This causes the lattice parameters of Mn-doped ZnO to increase, which increases the d values for each plane and causes the 2θ values to shift to a lower angle.

X-ray photoelectron spectroscopy

XPS was performed to identify the chemical composition and oxidation state of elements in ZnO and Mn-doped ZnO as shown in Fig. 5. A survey scan of ZnO showed peaks only for Zn 2p, O 1s and C 1s orbitals, showing the absence of any impurities. The survey scan of the Mn-doped ZnO showed an additional peak due to the Mn 2p orbital, indicating the doping of Mn in the ZnO. The doublet peaks for Zn $2p_{1/2}$ and Zn $2p_{3/2}$ in both microspheres are observed at 1045 and 1021.9 eV, respectively, as shown in Fig. 5a and separated by 23.1 eV, which agrees with the expected value for Zn^{2+}, as reported earlier [48,49].

Fig. 5b shows peaks at 655.2 and 642.0 eV correspond to Mn $2p_{1/2}$ and Mn $2p_{3/2}$, respectively, indicating the presence of Mn in a +2 oxidation state in Mn-doped ZnO [50]. The asymmetric O 1s spectra of pure ZnO are deconvoluted into two peaks at 532.7 and 530.7 eV as shown in Fig. 5c. The prominent O 1s peak at 530.7 eV corresponds to

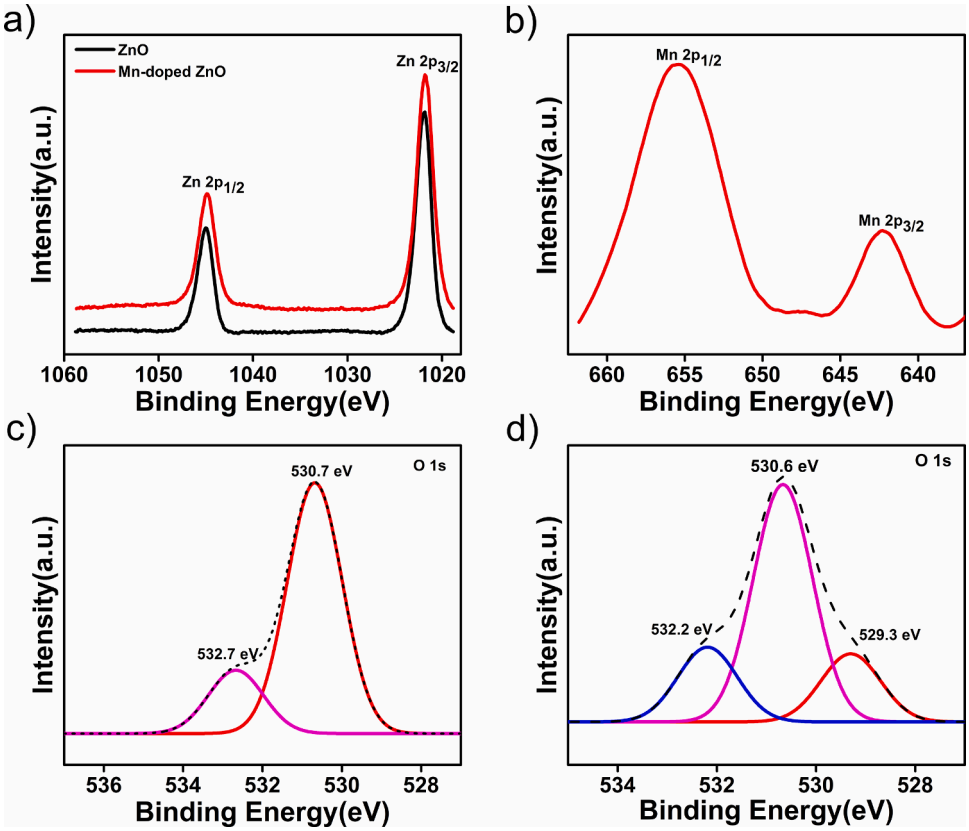

Fig. 5. (a) XPS spectra of the Zn 2p orbital of ZnO and Mn-doped ZnO. (b) XPS spectra of the Mn 2p orbital of Mn-doped ZnO. (c) XPS spectra of the O 1s orbital of ZnO. (d) XPS spectra of the O 1s orbital of Mn-doped ZnO.

lattice O^{2-} ions in the Zn–O bonding of the wurtzite structure of ZnO [51]. The peak at 532.7 eV is assigned to surface defects, oxygen vacancies, or chemisorbed oxygen species [52]. The O 1s spectra of Mn-doped ZnO as shown in Fig. 5d, deconvoluted into three peaks at 532.2, 530.6 and 529.3 eV. The peak at 530.6 is due to oxygen in the lattice. The peaks at 532.2 and 529.3 eV are assigned to oxygen vacancies and surface-adsorbed hydroxyl groups, respectively [53]. To understand the defects, the area under each peak in both the materials were calculated and compared. O 1s spectra of ZnO give an area of 79.84% for the lattice oxygen and the rest is for the surface defects, chemisorbed oxygen etc. In Mn-doped ZnO the lattice oxygen accounts for only 62.44% of the total area and the rest of the area denotes the defects including oxygen vacancies. This clearly shows that the Mn-doping in the ZnO lattice causes an increase in oxygen vacancies [54]. Oxygen vacancies are critical in gas sensing because the more oxygen vacancies, the more electrons can be trapped, and the gas detection performance of metal oxide sensors improves [55–57].

FTIR spectroscopy

FTIR spectra of the materials were recorded from 400 to 3000 cm^{-1} and are shown in Fig. 6a. The peak at 463 cm^{-1} in ZnO is due to the Zn-O stretching vibration and it confirms the formation of ZnO [58]. In Mn-doped ZnO, the broad peak at 492 cm^{-1} is assigned to the Mn-Zn-O stretching vibrations. The shift in the Zn-O stretching frequency is due to the incorporation of Mn into the ZnO lattice. This shift could be described in terms of atomic masses. Mn (54.93 u) has a smaller atomic mass than Zn (65.38 u), hence showing vibrational modes in the higher wavenumber range [59]. The shift to a higher wavenumber confirms the substitution of Mn ions in the ZnO lattice. The presence of atmospheric

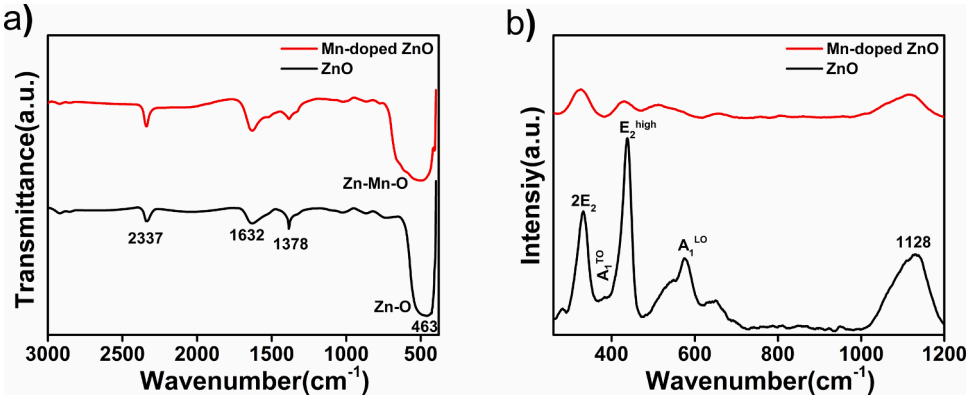

Fig. 6. (a) FTIR and (b) Raman spectra of ZnO and Mn-doped ZnO.

CO_2 gives a peak at 2337 cm^{-1} [60]. The peaks at 1378 and 1632 cm^{-1} correspond to the H-O-H bending mode [61,62] of a trace amount of water present on the surface of microspheres which results from atmospheric moisture [63].

Raman spectroscopy

Raman spectra of ZnO and Mn-doped ZnO microspheres were recorded in the range 200-1200 cm^{-1} to study the influence of Mn on the molecular vibrational modes of ZnO as shown in Fig. 6b. The strong band at 437 cm^{-1} in ZnO is assigned to the E_2 (high) mode, which predominantly involves Zn motion and is the characteristic band of the wurtzite phase. It confirms the formation of a ZnO wurtzite structure with P63mc symmetry. The vibrational modes at 331 cm^{-1} and 380 cm^{-1} correspond to $2E_2$ and A_1 (TO), respectively. The peak at 580 cm^{-1} corresponds to the A_1 (LO) mode in ZnO [64]. Corresponding peaks are also seen in Mn-doped ZnO indicating the wurtzite structure of Mn-doped ZnO. The intensity of E_2 (high) decreases in the Mn-doped ZnO due to the broken symmetry caused by Mn dopants in the ZnO lattice [65]. Substitution of Mn in the ZnO lattice causes structural perturbations in the periodic Zn atom sublattice and destroys the translational symmetry [66]. The broad band in the region of 1000-1200 cm^{-1} is originating from multi phonon processes [47].

Field emission scanning electron microscopy and energy-dispersive X-ray spectroscopy

FESEM micrographs of the ZnO and Mn-doped ZnO were acquired to analyse the morphology. The micrographs of the materials are shown in Fig. 7a and b. FESEM micrographs of ZnO and Mn-doped ZnO show spherical particles that are a few micrometers in size. ZnO has an average diameter of 10 μm, as shown in Fig. 7a. Whereas Mn-doped ZnO has an average particle size of 1 μm as shown in Fig. 7b. This indicates that Mn-doping reduced the particle size of ZnO microspheres. Mn-doping into the ZnO lattice does not change its morphology but reduces the particle size by inhibiting grain growth [60]. The surface of the Mn-doped ZnO was further analyzed by EDS and is shown in Fig. 7c. The EDS spectra showed the presence of Zn, Mn and O elements with weight percentages of 85.70, 2.02 and 12.28, respectively which also confirms the Mn-doping in ZnO and agrees with the doping percentage.

NH_3 and CO_2 temperature programmed desorption

NH_3 TPD was used to determine the number of acidic sites present on the surface of the ZnO and Mn-doped ZnO as shown in Fig. 8a. The area under the TPD spectra quantifies the acidic sites. The number of acidic sites on ZnO and Mn-doped ZnO are 0.016 and 0.073 mmol/g, respectively. It shows that doping with Mn increases the total number of acidic sites on the ZnO surface. In addition, CO_2 TPD was performed to assess the number of basic sites present on the material surface, as shown in Fig. 8b. The number of basic sites on the surface of ZnO and Mn-doped ZnO was calculated to be 0.021 and 0.067 mmol/g, respectively. Table 1 summarises the total acidic and basic sites present on the materials. The ratio of acidic to basic sites (S_a/S_b) was used to determine the catalytic nature of the surface. The S_a/S_b values of ZnO and Mn-doped ZnO are 0.761 and 1.089, respectively, indicating that acidic sites are more abundant in Mn-doped ZnO. Previous studies show that increasing the surface acidity of the sensor material favours the adsorption of basic gas molecules and can catalyze the reaction that occurs on the surface [42, 43]. The literature has also shown that the interaction between the

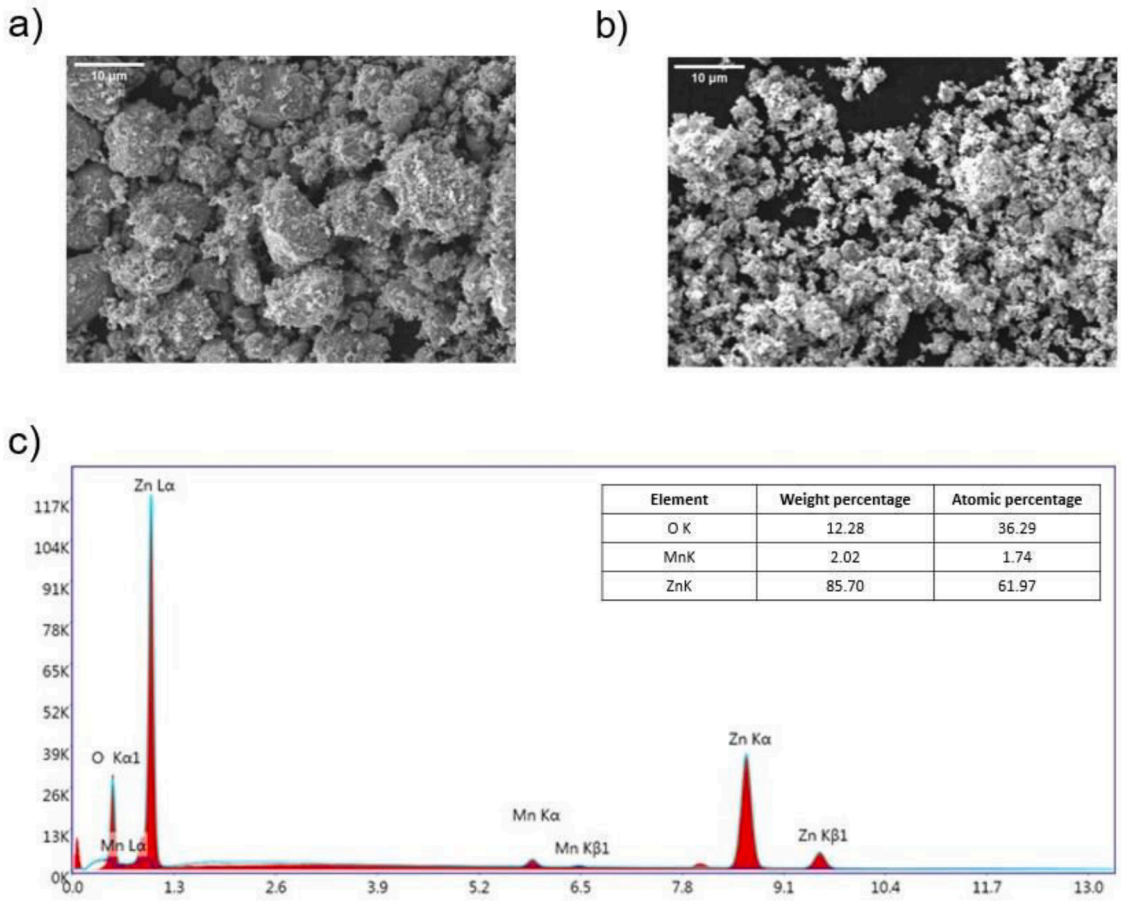

Fig. 7. (a) FESEM image of ZnO. (b) FESEM image of Mn-doped ZnO. (c) EDS spectrum of Mn-doped ZnO.

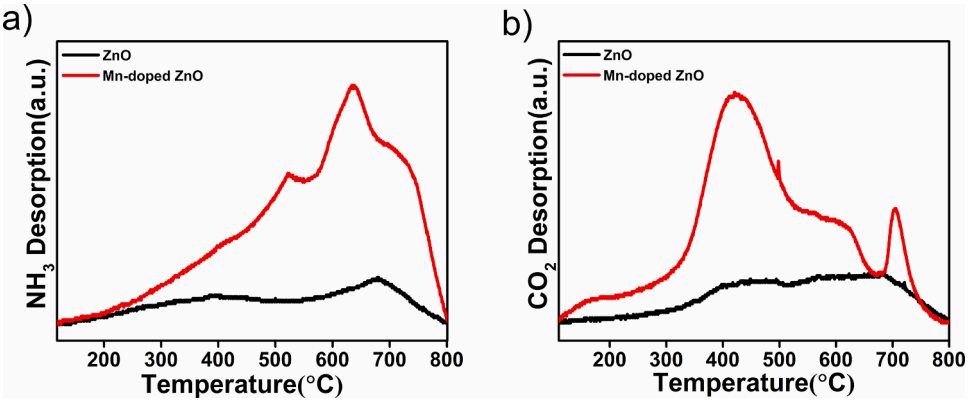

Fig. 8. (a) NH_3 TPD spectra of ZnO and Mn-doped ZnO. (b) CO_2 TPD spectra of ZnO and Mn-doped ZnO.

Table 1
Acidic and basic site quantification of the materials.

Material	Acidic sites (mmol/g) S_a	Basic sites (mmol/g) S_b	S_a/S_b
ZnO	0.016	0.021	0.761
Mn-doped ZnO	0.073	0.067	1.089

acidic surface sites and basic gas molecules leads to a selective determination of the gas [44,45]. Therefore, an increase in the surface acidity of Mn-doped ZnO is beneficial for more sensitive and selective determination of NH_3 gas.

Gas sensing studies

Fig. 9a, b show the change in resistance of ZnO and Mn-doped ZnO exposed to different concentrations of NH_3 gas at RT. In the presence of air, the microsphere exhibits a stable resistance and is recorded as the baseline resistance (R_a). When exposed to NH_3 gas, the resistance of the microspheres decreases and reaches a minimum value (R_g). After that, the microspheres are again exposed to air and the initial resistance value is restored. The resistance of ZnO and Mn-doped ZnO decreases in the presence of NH_3 and increases in air, showing n-type semiconductor behavior. ZnO had a baseline resistance of 4.8 MΩ, but the Mn-doped sample had an extremely high baseline resistance of 822.3 MΩ. The minimum resistance of the sensor steadily decreases with increasing NH_3 gas concentration, with the relative resistance change (R_a-R_g) being larger for Mn-doped ZnO than for ZnO. The response of the microspheres to NH_3 gas was estimated using the equation R_a/R_g. The gas sensing response of ZnO and Mn-doped ZnO to different NH_3 gas concentrations is shown in Fig. 9c. ZnO had a response of 1.6, 2.1, 3.3, and 6.6 at 25, 50, 75, and 100 ppm, respectively, while Mn-doped ZnO had a response of 3.7, 5.9, 11.5 and 20.2 at the same concentrations. Mn-doped ZnO shows greater response as compared to ZnO. Sensor response and recovery times are defined as the time required for the sensor to provide 90% of the final steady state signal in the presence of analyte gas and the time

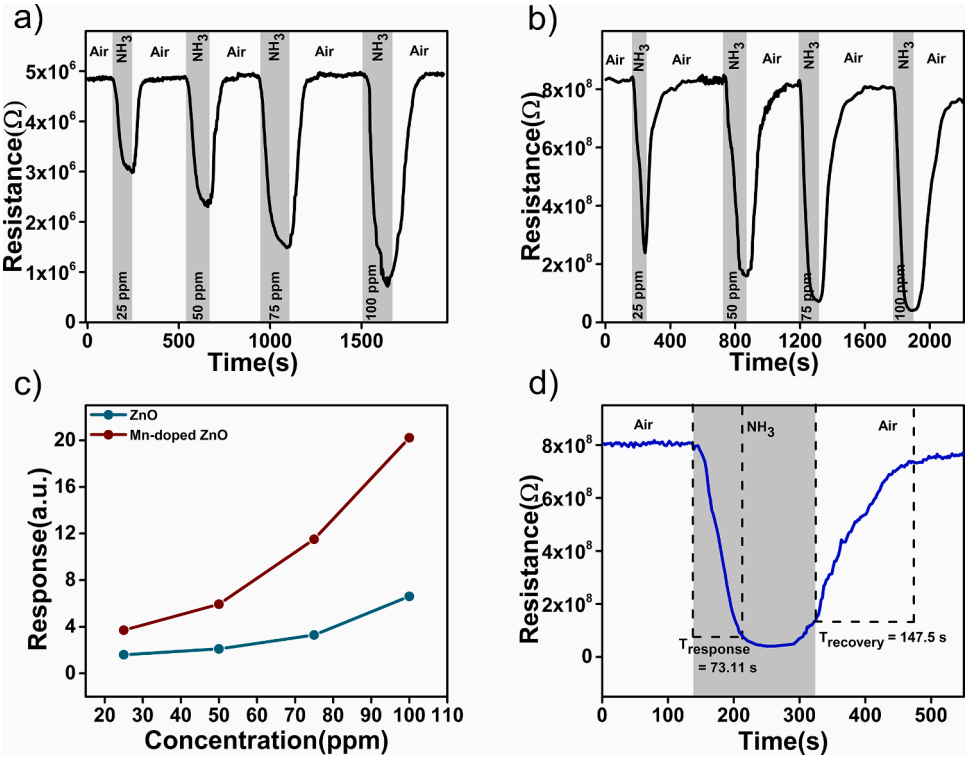

Fig. 9. Gas sensing studies (a) Resistance change of ZnO. (b) Resistance change of Mn-doped ZnO. (c) Response curve of ZnO and Mn-doped samples. (d) Response and recovery time of Mn-doped ZnO in 100 ppm concentration of NH_3 gas.

required for the sensor to reach 10% of the baseline resistance, respectively. For different concentrations of NH_3 gas, response and recovery time is calculated and is shown in Table 2. Mn-doped ZnO showed a shorter response time to NH_3 gas compared to ZnO, which is attributed to the better adsorption of NH_3 on the Mn-doped ZnO. However, because of stronger adsorption of NH_3 to Mn-doped ZnO, recovery time increases. The response and recovery time of Mn-doped ZnO towards 100 ppm NH_3 is shown in Fig. 9d.

The gas sensor responses of ZnO and Mn-doped ZnO at 100 ppm acetone, ethanol, formaldehyde (HCHO), and methanol are obtained and are shown in Fig. 10a. The response of the Mn-doped ZnO sensor to NH_3 was 20.2 to 100 ppm, which is substantially higher than the response to the same gas concentrations for other gases. This reveals the Mn-doped ZnO's remarkable selectivity towards NH_3. The calibration curve of the sensors is shown in Fig. 10b. Both ZnO and Mn-doped ZnO show a linear relationship between resistance and NH_3 concentration. The standard deviation of the baseline resistance (s) and the slope of the calibration curve (m) were used to calculate the limit of detection $\left(LOD = \frac{3s}{m}\right)$ which was found to be 3 and 12 ppm for ZnO and Mn-doped ZnO, respectively. Though Mn-doped ZnO is having high sensitivity, its LOD is found to be lower than ZnO. Fig. 10c shows the repeatability of the transient resistance curve of ZnO for four cycles of 100 ppm NH_3 injection over 1500 s. In all cycles the baseline resistance in air is restored and the minimum resistance reported for 100 ppm NH_3 is the same showing the repeatability of the measurements. The response of the ZnO and Mn-doped ZnO at a concentration of 100 ppm NH_3 was recorded over a period of 30 days and the sensors showed no appreciable drift in the response and showed excellent stability as shown in Fig. 10d.

Increased oxygen vacancies and increased surface acidity are the two effects that give Mn-doped ZnO better performance in terms of sensitivity, response, and selectivity to NH_3 gas. When Mn^{2+} replaces Zn^{2+} in the ZnO lattice, the lattice parameters change due to the size difference of the cations. Changing the lattice parameters increases the concentration of oxygen vacancies. An increase in oxygen vacancies increases chemisorbed oxygen at the surface. XPS studies showed that Mn-doped ZnO has a larger amount of chemisorbed oxygen formed by trapping charge carrying electrons from the conduction band. Increasing the chemisorbed oxygen drastically increases the baseline resistance of Mn-doped ZnO compared to ZnO. In the presence of NH_3 gas, the relative resistance change of Mn-doped ZnO is larger than ZnO and improves its sensitivity. Since NH_3 is a basic analyte gas, the acidic nature of the sensor material affects the sensing. From TPD, it is confirmed that Mn-doping increases the surface acidity of ZnO. The surface acidic sites on the Mn-doped ZnO are Lewis acidic sites and Bronsted acidic sites. Coordinatively unsaturated metal cations on the surface behave as Lewis acids and surface-adsorbed hydroxyl groups act as Bronsted acid sites. Lewis acidic sites facilitate the adsorption of basic NH_3 molecules by forming a coordination bond with the nitrogen lone pair. At the same time, polar NH_3 forms a hydrogen bond with the hydroxyl groups adsorbed on the surface. In this way, more NH_3 is adsorbed on the metal oxide surface. And this favors the reaction of NH_3 with chemisorbed oxygen. Acidic sites facilitate adsorption and catalyze the oxidation of NH_3 gas. As more NH_3 reacts with more oxygen gas, the resistance change increases and the response to NH_3 increases. Due to NH_3's ability to interact with the material, it results in highly selective sensing compared to other gases.

Table 2
Response and recovery time of materials towards NH_3 at RT.

Material	Time (s)	Concentration of NH_3 at RT (ppm)			
		25	50	75	100
ZnO	$T_{response}$	78.54	77.89	92.05	92.16
	$T_{recovery}$	64.16	67.46	88.35	146.05
Mn-doped ZnO	$T_{response}$	63.91	76.23	67.05	73.11
	$T_{recovery}$	197.35	160.56	189.36	147.50

A comparison of the NH_3 sensing performance of the Mn-doped ZnO with the previously reported transition metal doped ZnO sensors is shown in Table 3. Mn-doped ZnO has better sensor properties compared to other sensors at RT. Mn-doping has increased the response and selectivity of the ZnO sensor and lowered the operating temperature compared to other related ZnO sensors. Therefore, the Mn-doped ZnO is a promising candidate for RT NH_3 sensing.

Mechanism

The schematic sensing mechanism of the Mn-doped ZnO based NH_3 sensor is shown in Fig. 11. When the ZnO and Mn-doped ZnO gas sensors are present in the air, oxygen gas is chemically adsorbed on its surface by capturing the free electrons from its conduction band. This creates a charge carrier depleted region on the surface of the sensor, the resistance of which increases [67]. At lower temperatures, oxygen is mainly adsorbed as O_2^- species Eqs. (2) and (3) [68]. When the sensors are exposed to target gas, a chemical reaction occurs between oxygen with reducing NH_3 molecules Eqs. (4) and (5), and the previously trapped electrons are now released back into the semiconductor and the electrical resistance of the sensor decreases as the carrier concentration is increased.

$$O_2(in\ air) \rightarrow O_2(ads) \tag{2}$$

$$O_2(ads) + e^- \rightarrow O_2^-(ads) \tag{3}$$

$$NH_3(in\ air) \leftrightarrow NH_3(ads) \tag{4}$$

$$4NH_3(ads) + 3O_2^-(ads) \rightarrow 2N_2 + 6H_2O + 3e^- \tag{5}$$

The performance of the proposed NH_3 sensor is significantly influenced by the change in carrier concentration. According to the charge carrier concentration, the gas response, S (R_a/R_g), is defined as in Eq. (6) where $\Delta n = n_g - n_a$, and n_g, n_a represents the electron concentration in the sensor in the target gas and in the air, respectively [69].

$$S = \frac{\Delta n}{n_a} + 1 \tag{6}$$

The lower the electron concentration in air, the smaller n_a and the larger the variation in electron concentration Δn, resulting in a greater response against the reducing gas. Therefore, the improved sensing performance of Mn-doped ZnO could be explained by the following two aspects. The increased oxygen vacancy defect in Mn-doped ZnO enhances the donor effect, resulting in more surface adsorbed oxygen species and a thicker depletion layer, and therefore Mn-doped ZnO has a higher initial baseline resistance and large Δn value in the presence of NH_3, resulting in a higher response [70]. NH_3 adsorption on the surface, as shown in Eq. (4), is also a key step in the sensing mechanism. The acidic sites on the Mn-doped ZnO's surface facilitate the adsorption of more ammonia gas and catalyze the reaction between NH_3 and chemisorbed oxygen, increasing the sensitivity and selectivity of NH_3 sensing.

Conclusions

ZnO and 2 wt% Mn-doped ZnO microspheres were synthesized by solution combustion synthesis. The formation of the materials was confirmed by XRD, XPS, FTIR, RAMAN and EDS. Mn-doping slightly increases the lattice parameters of ZnO, as confirmed by XRD. The existence of Mn^{2+} and Zn^{2+} states in the Mn-doped ZnO was validated from XPS and increase in the oxygen vacancy in Mn-doped ZnO was also observed. FESEM images revealed the microsphere morphology of the materials, confirming that doping does not alter the morphology of ZnO. NH_3 and CO_2 TPD showed an increase in the surface acidic character of Mn-doped ZnO. At RT, Mn-doped ZnO showed a response of 20.2 towards 100 ppm NH_3 gas which is significantly higher than ZnO. Mn-doped ZnO sensor showed excellent selectivity compared to ZnO and

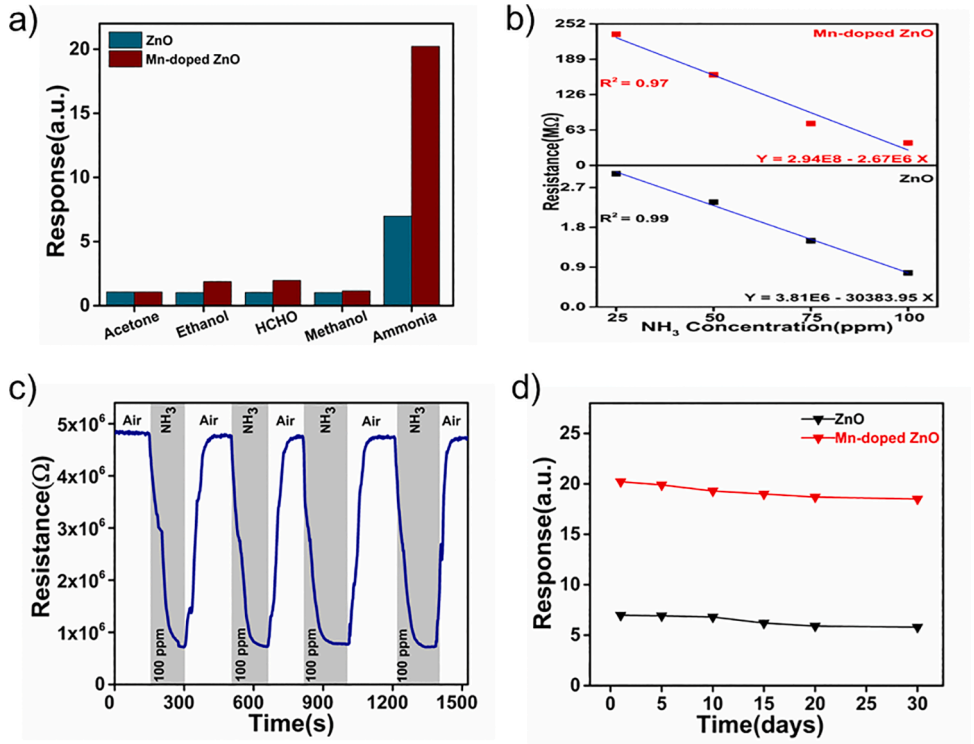

Fig. 10. (a) Selectivity study of ZnO and Mn-doped ZnO. (b) Linearity of the sensors. (c) Cycle repeatability of ZnO at 100 ppm concentration of NH_3. d) Long term stability of ZnO and Mn-doped ZnO.

Table 3
Comparison of transition metal doped ZnO sensors for NH_3 gas.

Material	Preparation technique	Working temperature (°C)	Concentration (ppm)	Response/S	Refs.
Co-ZnO thin film	Spray pyrolysis	25	100	3.48[a]	[40]
Ni-ZnO thin film	Spray pyrolysis	25	750	5[a]	[38]
Cd-ZnO thin film	Spray pyrolysis	325	100	5[b]	[37]
Ni-ZnO thin film	Spin coating	190	850	9.5[b]	[36]
Cu-ZnO nano flower	Hydrothermal synthesis	150	100	32.3[b]	[39]
Ag-ZnO nanostructured film	Magnetron sputtering	300	300	61.18[b]	[41]
Mn-ZnO microspheres	Solution combustion synthesis	25	100	20.22[a] 95.37[b]	This work

$S^a = R_a/R_g$, $S^b = (R_a - R_g) \times 100/R_a$

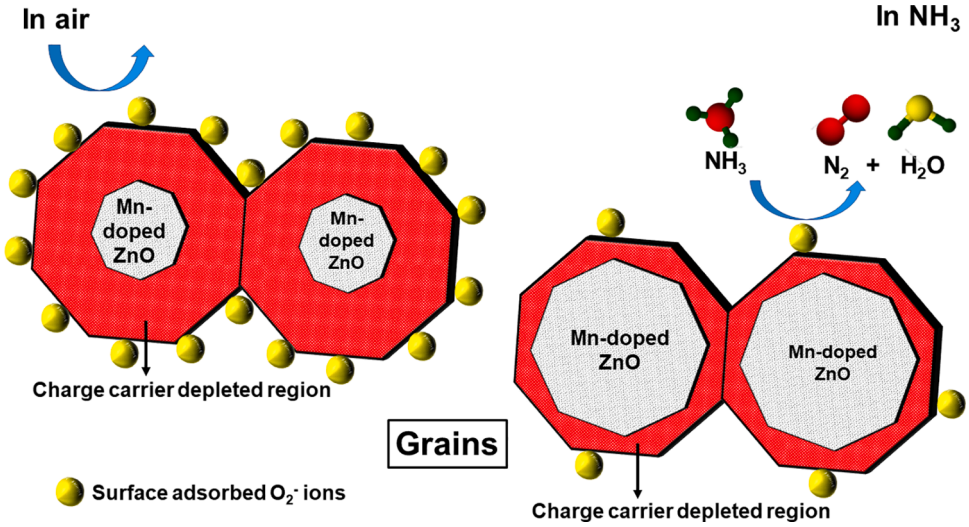

Fig. 11. Schematic representation for the NH_3 gas sensing Mechanism of Mn-doped ZnO.

exhibits good stability. The improvement in the gas sensing performance of Mn-doped ZnO is mainly due to the increase in the surface defect and surface acidity. Mn-doping increased oxygen vacancies and enhanced chemisorbed oxygen species on the surface, resulting in an increase in baseline resistance and gas sensing response. In addition, Mn-doping increases the number of acidic sites which favours the adsorption of more amount of basic NH_3 gas and catalyzes the surface reaction increasing the response and selectivity to basic NH_3 gas.

Declaration of Competing Interest

The authors declare that they have no known competing financial interests or personal relationships that could have appeared to influence the work reported in this paper.

Data Availability

Data will be made available on request.

Acknowledgments

Asha Ramesh wishes to express her gratitude to the Innovation in Science Pursuit for Inspired Research (INSPIRE) initiative of the Department of Science and Technology (DST), Government of India, for granting a Ph.D. research fellowship that allowed her to complete this project in a timely manner.

References

[1] R. Patnaik, Impact of industrialization on environment and sustainable solutions – reflections from a south Indian region, IOP Conf. Ser. Earth Environ. Sci. 120 (2018), 012016, https://doi.org/10.1088/1755-1315/120/1/012016.
[2] D. Kwak, Y. Lei, R. Maric, Ammonia gas sensors: a comprehensive review, Talanta 204 (2019) 713–730, https://doi.org/10.1016/j.talanta.2019.06.034.
[3] M. Serafini, F. Mariani, I. Gualandi, F. Decataldo, L. Possanzini, M. Tessarolo, B. Fraboni, D. Tonelli, E. Scavetta, A wearable electrochemical gas sensor for ammonia detection, Sensors 21 (2021) 7905, https://doi.org/10.3390/s21237905.
[4] B. Tsizh, O. Aksimentyeva, Ways to improve the parameters of optical gas sensors of ammonia based on polyaniline, Sens. Actuators A Phys. 315 (2020), 112273, https://doi.org/10.1016/j.sna.2020.112273.
[5] P.N. Bartlett, S. Guerin, A micromachined calorimetric gas sensor: an application of electrodeposited nanostructured palladium for the detection of combustible gases, Anal. Chem. 75 (2003) 126–132, https://doi.org/10.1021/ac026141w.
[6] S. Kanan, O. El-Kadri, I. Abu-Yousef, M. Kanan, Semiconducting metal oxide based sensors for selective gas pollutant detection, Sensors 9 (2009) 8158–8196, https://doi.org/10.3390/s91008158.
[7] S.H. Wang, C.Y. Shen, J.M. Su, S.W. Chang, A room temperature nitric oxide gas sensor based on a copper-ion-doped polyaniline/tungsten oxide nanocomposite, Sensors 15 (2015) 7084–7095, https://doi.org/10.3390/s150407084.
[8] Q. Xue, H. Chen, Q. Li, K. Yan, F. Besenbacher, M. Dong, Room-temperature high-sensitivity detection of ammonia gas using the capacitance of carbon/silicon heterojunctions, Energy Environ. Sci. 3 (2010) 288, https://doi.org/10.1039/b925172n.
[9] G. Scholl, F. Schmidt, U. Wolff, Surface acoustic wave devices for sensor applications, Phys. Status Solidi (a) 185 (2001) 47–58, https://doi.org/10.1002/1521-396X(200105)185:1<47::AID-PSSA47>3.0.CO;2-Q.
[10] G. Korotcenkov, B.K. Cho, Metal oxide composites in conductometric gas sensors: achievements and challenges, Sens. Actuators B Chem. 244 (2017) 182–210, https://doi.org/10.1016/j.snb.2016.12.117.
[11] C. Wang, X. Cui, J. Liu, X. Zhou, X. Cheng, P. Sun, X. Hu, X. Li, J. Zheng, G. Lu, Design of superior ethanol gas sensor based on Al-Doped NiO Nanorod-flowers, ACS Sens. 1 (2016) 131–136, https://doi.org/10.1021/acssensors.5b00123.
[12] Z.L. Wang, Splendid one-dimensional nanostructures of zinc oxide: a new nanomaterial family for nanotechnology, ACS Nano 2 (2008) 1987–1992, https://doi.org/10.1021/nn800631r.
[13] C. Li, Z. Du, H. Yu, T. Wang, Low-temperature sensing and high sensitivity of ZnO nanoneedles due to small size effect, Thin. Solid. Films 517 (2009) 5931–5934, https://doi.org/10.1016/j.tsf.2009.04.025.
[14] D. Wang, D. Zhang, Y. Yang, Q. Mi, J. Zhang, L. Yu, Multifunctional latex/polytetrafluoroethylene-based triboelectric nanogenerator for self-powered organ-like mxene/metal–organic framework-derived CuO nanohybrid ammonia sensor, ACS Nano 15 (2021) 2911–2919, https://doi.org/10.1021/acsnano.0c09015.
[15] S. Jayawardena, A. Kubono, R.M.G. Rajapakse, M. Shimomura, Effect of titanium precursors used in the preparation of graphene oxide/TiO_2 composite for gas sensing utilizing quartz crystal microbalance, Nano-Struct. Nano Objects 28 (2021), 100780, https://doi.org/10.1016/j.nanoso.2021.100780.
[16] S. Zinatloo-Ajabshir, M.S. Morassaei, O. Amiri, M. Salavati-Niasari, L.K. Foong, $Nd_2Sn_2O_7$ nanostructures: green synthesis and characterization using date palm extract, a potential electrochemical hydrogen storage material, Ceram. Int. 46 (2020) 17186–17196, https://doi.org/10.1016/j.ceramint.2020.03.014.
[17] M. Amiri, M. Salavati-Niasari, A. Pardakhty, M. Ahmadi, A. Akbari, Caffeine: a novel green precursor for synthesis of magnetic $CoFe_2O_4$ nanoparticles and pH-sensitive magnetic alginate beads for drug delivery, Mater. Sci. Eng. C 76 (2017) 1085–1093, https://doi.org/10.1016/j.msec.2017.03.208.
[18] S. Mersagh Dezfuli, M. Sabzi, Deposition of self-healing thin films by the sol–gel method: a review of layer-deposition mechanisms and activation of self-healing mechanisms, Appl. Phys. A 125 (2019) 557, https://doi.org/10.1007/s00339-019-2854-8.
[19] M. Sabzi, S.H. Mousavi Anijdan, Microstructural analysis and optical properties evaluation of sol-gel heterostructured NiO-TiO_2 film used for solar panels, Ceram. Int. 45 (2019) 3250–3255, https://doi.org/10.1016/j.ceramint.2018.10.229.
[20] S. Mersagh Dezfuli, M. Sabzi, A study on the effect of presence of CeO_2 and benzotriazole on activation of self-healing mechanism in ZrO_2 ceramic-based coating, Int. J. Appl. Ceram. Technol. 15 (2018) 1248–1260, https://doi.org/10.1111/ijac.12901.
[21] S.M. Dezfuli, M. Sabzi, Effect of yttria and benzotriazole doping on wear/corrosion responses of alumina-based nanostructured films, Ceram. Int. 44 (2018) 20245–20258, https://doi.org/10.1016/j.ceramint.2018.07.313.
[22] R. Monsef, M. Salavati-Niasari, Hydrothermal architecture of $Cu_5V_2O_{10}$ nanostructures as new electro-sensing catalysts for voltammetric quantification of mefenamic acid in pharmaceuticals and biological samples, Biosens. Bioelectron. 178 (2021), 113017, https://doi.org/10.1016/j.bios.2021.113017.
[23] R. Monsef, M. Salavati-Niasari, M. Masjedi-Arani, Hydrothermal synthesis of spinel-perovskite Li–Mn–Fe–Si nanocomposites for electrochemical hydrogen storage, Inorg. Chem. 61 (2022) 6750–6763, https://doi.org/10.1021/acs.inorgchem.1c03605.
[24] F. Motahari, M.R. Mozdianfard, M. Salavati-Niasari, Synthesis and adsorption studies of NiO nanoparticles in the presence of H2acacen ligand, for removing Rhodamine B in wastewater treatment, Process Saf. Environ. Prot. 93 (2015) 282–292, https://doi.org/10.1016/j.psep.2014.06.006.
[25] S. Zinatloo-Ajabshir, M. Salavati-Niasari, Preparation of magnetically retrievable $CoFe_2O_4$@SiO_2@$Dy_2Ce_2O_7$ nanocomposites as novel photocatalyst for highly efficient degradation of organic contaminants, Compos. B Eng. 174 (2019), 106930, https://doi.org/10.1016/j.compositesb.2019.106930.
[26] G.N. Dar, A. Umar, S.A. Zaidi, S. Baskoutas, S.W. Hwang, M. Abaker, A. Al-Hajry, S. A. Al-Sayari, Ultra-high sensitive ammonia chemical sensor based on ZnO nanopencils, Talanta 89 (2012) 155–161, https://doi.org/10.1016/J.TALANTA.2011.12.006.
[27] J. Samà, S. Barth, G. Domènech-Gil, J.D. Prades, N. López, O. Casals, I. Gràcia, C. Cané, A. Romano-Rodríguez, Site-selectively grown SnO_2 NWs networks on micromembranes for efficient ammonia sensing in humid conditions, Sens. Actuators B Chem. 232 (2016) 402–409, https://doi.org/10.1016/J.SNB.2016.03.091.
[28] X. Li, N. Chen, S. Lin, J. Wang, J. Zhang, NiO-wrapped mesoporous TiO_2 microspheres based selective ammonia sensor at room temperature, Sens. Actuators B Chem. 209 (2015) 729–734, https://doi.org/10.1016/J.SNB.2014.12.031.
[29] S. Büyükköse, Highly selective and sensitive WO3 nanoflakes based ammonia sensor, Mater. Sci. Semicond. Process. 110 (2020), 104969, https://doi.org/10.1016/J.MSSP.2020.104969.
[30] D. Kwak, M. Wang, K.J. Koski, L. Zhang, H. Sokol, R. Maric, Y. Lei, Molybdenum trioxide (α-MoO $_3$) nanoribbons for ultrasensitive ammonia (NH_3) gas detection: integrated experimental and density functional theory simulation studies, ACS Appl. Mater. Interfaces 11 (2019) 10697–10706, https://doi.org/10.1021/acsami.8b20502.
[31] Y. Kang, F. Yu, L. Zhang, W. Wang, L. Chen, Y. Li, Review of ZnO-based nanomaterials in gas sensors, Solid State Ion. 360 (2021), 115544, https://doi.org/10.1016/j.ssi.2020.115544.
[32] V.S. Bhati, M. Hojamberdiev, M. Kumar, Enhanced sensing performance of ZnO nanostructures-based gas sensors: a review, Energy Rep. 6 (2020) 46–62, https://doi.org/10.1016/j.egyr.2019.08.070.
[33] C.L. Hsu, L.F. Chang, T.J. Hsueh, Light-activated humidity and gas sensing by ZnO nanowires grown on LED at room temperature, Sens. Actuators B Chem. 249 (2017) 265–277, https://doi.org/10.1016/j.snb.2017.04.083.
[34] J. Xuan, G. Zhao, M. Sun, F. Jia, X. Wang, T. Zhou, G. Yin, B. Liu, Low-temperature operating ZnO-based NO $_2$ sensors: a review, RSC Adv. 10 (2020) 39786–39807, https://doi.org/10.1039/D0RA07328H.
[35] K. Shingange, Z.P. Tshabalala, O.M. Ntwaeaborwa, D.E. Motaung, G.H. Mhlongo, Highly selective NH_3 gas sensor based on Au loaded ZnO nanostructures prepared using microwave-assisted method, J. Colloid Interface Sci. 479 (2016) 127–138, https://doi.org/10.1016/j.jcis.2016.06.046.
[36] A.P. Rambu, L. Ursu, N. Iftimie, V. Nica, M. Dobromir, F. Iacomi, Study on Ni-doped ZnO films as gas sensors, Appl. Surf. Sci. 280 (2013) 598–604, https://doi.org/10.1016/J.APSUSC.2013.05.033.
[37] N.L. Tarwal, A.R. Patil, N.S. Harale, A.V. Rajgure, S.S. Suryavanshi, W.R. Bae, P. S. Patil, J.H. Kim, J.H. Jang, Gas sensing performance of the spray deposited Cd-ZnO thin films, J. Alloys Compd. 598 (2014) 282–288, https://doi.org/10.1016/J.JALLCOM.2014.01.200.
[38] G.K. Mani, J.B.B. Rayappan, Selective detection of ammonia using spray pyrolysis deposited pure and nickel doped ZnO thin films, Appl. Surf. Sci. 311 (2014) 405–412, https://doi.org/10.1016/J.APSUSC.2014.05.075.

[39] R.S. Ganesh, E. Durgadevi, M. Navaneethan, V.L. Patil, S. Ponnusamy, C. Muthamizhchelvan, S. Kawasaki, P.S. Patil, Y. Hayakawa, Tuning the selectivity of NH_3 gas sensing response using Cu-doped ZnO nanostructures, Sens. Actuators A Phys. 269 (2018) 331–341, https://doi.org/10.1016/J.SNA.2017.11.042.
[40] G.K. Mani, J.B.B. Rayappan, A highly selective and wide range ammonia sensor – nanostructured ZnO: Co thin film, Mater. Sci. Eng. B 191 (2015) 41–50, https://doi.org/10.1016/j.mseb.2014.10.007.
[41] Y. Zheng, M. Li, X. Wen, H.P. Ho, H. Lu, Nanostructured ZnO/Ag film prepared by magnetron sputtering method for fast response of ammonia gas detection, Molecules 25 (2020) 1899, https://doi.org/10.3390/molecules25081899.
[42] M.N. Rumyantseva, A.M. Gas'kov, Chemical modification of nanocrystalline metal oxides: effect of the real structure and surface chemistry on the sensor properties, Russ. Chem. Bull. 57 (2008) 1106–1125, https://doi.org/10.1007/s11172-008-0139-z.
[43] N. Vorobyeva, M. Rumyantseva, D. Filatova, E. Konstantinova, D. Grishina, A. Abakumov, S. Turner, A. Gaskov, Nanocrystalline ZnO(Ga): paramagnetic centers, surface acidity and gas sensor properties, Sens. Actuators B Chem. 182 (2013) 555–564, https://doi.org/10.1016/j.snb.2013.03.068.
[44] A. Satsuma, M. Katagiri, S. Kakimoto, S. Sugaya, K. Shimizu, Effects of calcination temperature and acid-base properties on mixed potential ammonia sensors modified by metal oxides, Sensors 11 (2011) 2155–2165, https://doi.org/10.3390/s110202155.
[45] Y. Seekaew, W. Pon-On, C. Wongchoosuk, Ultrahigh selective room-temperature ammonia gas sensor based on tin–titanium dioxide/reduced graphene/carbon nanotube nanocomposites by the solvothermal method, ACS Omega 4 (2019) 16916–16924, https://doi.org/10.1021/acsomega.9b02185.
[46] G.H. Mhlongo, K. Shingange, Z.P. Tshabalala, B.P. Dhonge, F.A. Mahmoud, B. W. Mwakikunga, D.E. Motaung, Room temperature ferromagnetism and gas sensing in ZnO nanostructures: Influence of intrinsic defects and Mn, Co, Cu doping, Appl. Surf. Sci. 390 (2016) 804–815, https://doi.org/10.1016/J.APSUSC.2016.08.138.
[47] K.V.A. Kumar, S.R. Amanchi, B. Sreedhar, P. Ghosal, Ch. Subrahmanyam, Phenol and Cr(<scp>vi</scp>) degradation with Mn ion doped ZnO under visible light photocatalysis, RSC Adv. 7 (2017) 43030–43039, https://doi.org/10.1039/C7RA08172C.
[48] R.Devi Chandra, K.G. Gopchandran, Simple, low-temperature route to synthesize ZnO nanoparticles and their optical neuromorphic characteristics, ACS Appl Electron Mater 3 (2021) 3846–3854, https://doi.org/10.1021/acsaelm.1c00471.
[49] M. Claros, M. Setka, Y.P. Jimenez, S. Vallejos, AACVD synthesis and characterization of iron and copper oxides modified ZnO structured films, Nanomaterials 10 (2020) 471, https://doi.org/10.3390/nano10030471.
[50] D. Wang, W. Shang, B. Zhang, C. Jiang, F. Qu, M. Yang, Manganese-doped zinc oxide hollow balls for chemiresistive sensing of acetone vapors, Microchim. Acta 186 (2019) 44, https://doi.org/10.1007/s00604-018-3108-8.
[51] F.M. Chang, S. Brahma, J.H. Huang, Z.Z. Wu, K.Y. Lo, Strong correlation between optical properties and mechanism in deficiency of normalized self-assembly ZnO nanorods, Sci. Rep. 9 (2019) 905, https://doi.org/10.1038/s41598-018-37601-8.
[52] Y.H. Duan, Y. Duan, P. Chen, Y. Tao, Y.Q. Yang, Y. Zhao, High-performance flexible Ag nanowire electrode with low-temperature atomic-layer-deposition fabrication of conductive-bridging ZnO film, Nanoscale Res. Lett. 10 (2015) 90, https://doi.org/10.1186/s11671-015-0810-x.
[53] V. Strelchuk, O. Kolomys, S. Rarata, P. Lytvyn, O. Khyzhun, C.O. Chey, O. Nur, M. Willander, Raman submicron spatial mapping of individual Mn-doped ZnO nanorods, Nanoscale Res. Lett. 12 (2017) 351, https://doi.org/10.1186/s11671-017-2127-4.
[54] M. Shatnawi, A.M. Alsmadi, I. Bsoul, B. Salameh, M. Mathai, G. Alnawashi, G. M. Alzoubi, F. Al-Dweri, M.S. Bawa'aneh, Influence of Mn doping on the magnetic and optical properties of ZnO nanocrystalline particles, Results Phys. 6 (2016) 1064–1071, https://doi.org/10.1016/j.rinp.2016.11.041.
[55] Y. Ge, Z. Wei, Y. Li, J. Qu, B. Zu, X. Dou, Highly sensitive and rapid chemiresistive sensor towards trace nitro-explosive vapors based on oxygen vacancy-rich and defective crystallized In-doped ZnO, Sens. Actuators B Chem. 244 (2017) 983–991, https://doi.org/10.1016/j.snb.2017.01.092.
[56] M. Al-Hashem, S. Akbar, P. Morris, Role of oxygen vacancies in nanostructured metal-oxide gas sensors: a review, Sens. Actuators B Chem. 301 (2019), 126845, https://doi.org/10.1016/j.snb.2019.126845.
[57] W. Kim, M. Choi, K. Yong, Generation of oxygen vacancies in ZnO Nanorods/films and their effects on gas sensing properties, Sens. Actuators B Chem. 209 (2015) 989–996, https://doi.org/10.1016/j.snb.2014.12.072.
[58] B.N. Dole, V.D. Mote, V.R. Huse, Y. Purushotham, M.K. Lande, K.M. Jadhav, S. S. Shah, Structural studies of Mn doped ZnO nanoparticles, Curr. Appl. Phys. 11 (2011) 762–766, https://doi.org/10.1016/J.CAP.2010.11.050.
[59] Z.N. Kayani, M. Anjum, S. Riaz, S. Naseem, T. Zeeshan, Role of Mn in biological, optical, and magnetic properties ZnO Nano-particles, Appl. Phys. A 126 (2020) 197, https://doi.org/10.1007/s00339-020-3380-4.
[60] S. Senthilkumaar, K. Rajendran, S. Banerjee, T.K. Chini, V. Sengodan, Influence of Mn doping on the microstructure and optical property of ZnO, Mater. Sci. Semicond. Process. 11 (2008) 6–12, https://doi.org/10.1016/j.mssp.2008.04.005.
[61] K.V.A. Kumar, T. Vinodkumar, M. Selvaraj, D. Suryakala, C. Subrahmanyam, Visible light-induced catalytic abatement of 4-nitrophenol and Rhodamine B using ZnO/g-C_3N_4 catalyst, J. Chem. Sci. 133 (2021) 41, https://doi.org/10.1007/s12039-021-01903-8.
[62] C. Belkhaoui, N. Mzabi, H. Smaoui, Investigations on structural, optical and dielectric properties of Mn doped ZnO nanoparticles synthesized by co-precipitation method, Mater. Res. Bull. 111 (2019) 70–79, https://doi.org/10.1016/J.MATERRESBULL.2018.11.006.
[63] D. Anbuselvan, S. Muthukumaran, Defect related microstructure, optical and photoluminescence behaviour of Ni, Cu co-doped ZnO nanoparticles by co-precipitation method, Opt. Mater. (Amst) 42 (2015) 124–131, https://doi.org/10.1016/J.OPTMAT.2014.12.030.
[64] A.C. Lucilha, R. Afonso, P.R.C. Silva, L.F. Lepre, R.A. Ando, L.H. Dall'Antonia, ZnO prepared by solution combustion synthesis: characterization and application as photoanode, J. Braz. Chem. Soc. (2014), https://doi.org/10.5935/0103-5053.20140085.
[65] J.B. Wang, G.J. Huang, X.L. Zhong, L.Z. Sun, Y.C. Zhou, E.H. Liu, Raman scattering and high temperature ferromagnetism of Mn-doped ZnO nanoparticles, Appl. Phys. Lett. 88 (2006), 252502, https://doi.org/10.1063/1.2208564.
[66] Q. Gao, Y. Dai, C. Li, L. Yang, X. Li, C. Cui, Correlation between oxygen vacancies and dopant concentration in Mn-doped ZnO nanoparticles synthesized by co-precipitation technique, J. Alloys Compd. 684 (2016) 669–676, https://doi.org/10.1016/j.jallcom.2016.05.227.
[67] P. Sun, X. Zhou, C. Wang, B. Wang, X. Xu, G. Lu, One-step synthesis and gas sensing properties of hierarchical Cd-doped SnO_2 nanostructures, Sens. Actuators B Chem 190 (2014) 32–39, https://doi.org/10.1016/j.snb.2013.08.045.
[68] D. Wei, Z. Huang, L. Wang, X. Chuai, S. Zhang, G. Lu, Hydrothermal synthesis of Ce-doped hierarchical flower-like In_2O_3 microspheres and their excellent gas-sensing properties, Sens. Actuators B Chem 255 (2018) 1211–1219, https://doi.org/10.1016/j.snb.2017.07.162.
[69] H.J. Kim, K.I. Choi, K.M. Kim, C.W. Na, J.H. Lee, Highly sensitive C_2H_5OH sensors using Fe-doped NiO hollow spheres, Sens. Actuators B Chem. 171–172 (2012) 1029–1037, https://doi.org/10.1016/j.snb.2012.06.029.
[70] K. Wu, M. Debliquy, C. Zhang, Room temperature gas sensors based on Ce doped TiO_2 nanocrystals for highly sensitive NH_3 detection, Chem. Eng. J. 444 (2022), 136449, https://doi.org/10.1016/j.cej.2022.136449.